A Comparative Analysis of Index-Based Methods for Impervious Surface Mapping Using Multiseasonal Sentinel-2 Satellite Data

Congmin Li ©, Zhenfeng Shao ©, Lei Zhang ©, Xiao Huang, and Ming Zhang

Abstract—Studies have shown that Sentinel-2 images have advantages over Landsat images in impervious surface area (ISA) extraction. The performance of index-based methods can be affected by different binary methods and subject to seasonal variation. This study marks the first attempt to assess the performance of different spectral indices for ISA extraction using multiseasonal Sentinel-2 images. Specifically, five indices (i.e., the biophysical composition index calculated using the Gram–Schmidt orthogonalization method, biophysical composition index calculated using a principal component-based Procrustes analysis, Normalized Built-up Area Index (NBAI), combinational build-up index, and perpendicular impervious surface index (PISI)) and three impervious surface binary methods (i.e., Otsu's method, manual method, and Iterative Self-Organizing Data Analysis Technique Algorithm (ISODATA) classification method) were tested on multi-seasonal Sentinel-2 images in the main urban area of Wuhan, China. Results showed that PISI combined with the ISODATA classification method achieved the highest accuracy with 92.64% OA, and 0.8410 Kappa coefficient, and NBAI combined with Otsu's method achieved the lowest accuracy with 35.37% OA, and 0.013 Kappa coefficient. Regarding the seasonal sensitivity, PISI is relatively more stable than the other methods. The superior performance of PISI is largely due to its capability in separating ISA from soil and vegetation. In addition, summer is the best season to map ISA from Sentinel-2 images when the impervious surface is generally less confused with bare soil. This study serves as a reference for the selection of spectral indices for ISA extraction from Sentinel-2 images in relation to binary methods and seasonal effects.

Index Terms—Impervious surface, index-based methods, seasonal effect, sentinel-2, urban indices.

Congmin Li and Zhenfeng Shao are with the State Key Laboratory for Information Engineering in Surveying, Mapping and Remote Sensing, Wuhan University, Wuhan 430079, China (e-mail: cminlee@whu.edu.cn; shaozhenfeng@whu.edu.cn).

Lei Zhang is with the School of Remote Sensing and Information Engineering, Wuhan University, Wuhan 430079, China, and also with Key Laboratory of Urban Land Resources Monitoring and Simulation, Ministry of Natural Resources, Shenzhen 518034, China (e-mail: zhanglei1990@whu.edu.cn).

Xiao Huang is with the Department of Geosciences, University of Arkansas, Fayetteville, AR 72701 USA (e-mail: xh010@uark.edu).

Ming Zhang is with the School of Resources and Environmental Engineering, Wuhan University of Technology, Wuhan 430070, China (e-mail: zhangming_88@whut.edu.cn).

I. INTRODUCTION

IMPERVIOUS surfaces include man-made surfaces, such as roads, driveways, sidewalks, parking lots, rooftops, which prevent water from infiltrating into the soil [1]. Over time, impervious surface area (ISA) has been experiencing dramatic expansion with rapid urbanization [2], which potentially leads to negative ecological and environmental consequences, such as urban heat island [3]–[5] and waterlogging [6]. Therefore, timely and accurate ISA mapping plays a crucial role in urban planning and ecological environment assessment.

With the advancement of remote sensing technology, satellite images have become one of the key data sources for mapping and monitoring ISA dynamics [7]. Commonly used remotely sensed data include MODIS [8], [9], Landsat [10], Sentinel-2 [11], [12], IKONOS [13], [14], to list a few. As medium-resolution images can provide reliable ISA estimations [1], 30 m Landsat products have been widely used to extract and characterize the dynamics of impervious surfaces [2], [7], [9]. Nevertheless, ISA extracted from Landsat data is insufficient to describe urban biophysical components [15], [16]. Compared to Landsat, Sentinel-2 satellites are able to acquire images with a spatial resolution of 10–60 m every ten days, creating new opportunities for accurate and detailed urban ISA mapping. Efforts have been made to investigate ISA extraction from Sentinel-2 imagery. Xu *et al*. [12] presented a modified linear spectral mixture method to extract a high-resolution (10 m) impervious surface map from Sentinel-2 images, in which roads and the boundaries of buildings could be clearly identified. Xian *et al*. [17] evaluated performances of WorldView-3, Sentinel-2, and Landsat-8 data in ISA mapping. Their conclusion suggests that results extracted from Sentinel-2 images are similar to those from WorldView-3. In comparison, Landsat images produced results with the lowest accuracy because they have fewer spectral bands and lower spatial resolution. Performances of Sentinel-2 and Landsat-8 images in ISA extraction were assessed using different methods. The experimental results revealed that more details and higher accuracy ISA are obtained from Sentinel-2 images [18]. Misra *et al*. [11] evaluated the performances of three supervised classification methods for the generation of land use and land cover maps from Sentinel-2 images. In addition, they

made a zonal analysis to understand the impacts of extracted built-up impervious surfaces on rising environmental issues. These efforts suggest that Sentinel-2 imagery is a valid source for land cover classification and ISA mapping, given its fine spatial resolution and free access.

In recent years, numerous methods have been developed to map ISA using remotely sensed data, including classification-based [19], [20], mixture analysis [21], [22], and index-based methods [23]–[26]. Among all the discussed methods, the index-based method is the most commonly used method for ISA mapping, as it is implementation-friendly and largely parameter-free. In general, an index-based ISA extraction method finds the strongest reflection band and the weakest reflection band of the impervious surface in multispectral images, and expands the intensity contrast between the impervious surface and the background through mathematical operations on selected bands [26]. Typical indices include (but are not limited to) normalized difference built-up index (NDBI) [27], index-based built-up index (IBI) [28], normalized difference impervious surface index (NDISI) [26], new built-up index (NBI) [29], biophysical composition index (BCI) [23], normalized built-up area index (NBAI) [30], modified built-up index (MBI) [31], normalized difference impervious index (NDII) [32], combinational build-up index (CBI) [33], modified NDISI (MNDISI) [34], and perpendicular impervious surface index (PISI) [25].

These indices are designed primarily for Landsat imagery. Some indices, however, may not be feasible for other satellites due to band discrepancies. For instance, NDISI, NDII, and MNDISI cannot be used in Sentinel-2 images as the construction of these indices requires a thermal infrared band, which is not covered by the Sentinel-2 MSI sensor. Despite the existing studies that assessed the performances of various indices for ISA mapping on Landsat images [35], [36], only a few studies have evaluated the performance of the impervious surface indices on Sentinel-2 imagery. Deliry *et al.* [18] applied both supervised classification methods and two band-ratioing methods (NDBI and NDII) to extract ISA from Sentinel-2 and Landsat-8 data. Only the performance of NDBI, however, was assessed using Sentinel-2 images. Tang *et al.* [37] developed a new ISA extraction method using JL1-3B Nighttime Light and Sentinel-2 Image. In their study, NDBI and BCI were used to evaluate the extraction performance. Experimental results showed that BCI outperformed NDBI. Despite these attempts, the two investigations on the accuracy of index-based methods using Sentinel-2 data were not comprehensive. One notable effort by Chen *et al.* [38] investigated the performances of six index-based methods using Sentinel-2 data. However, their study failed to consider the potential influence of seasonal variation on the performance of these indices.

To generate an impervious surface thematic map for spatial and quantitative analysis, the calculated index images need to be reclassified as either impervious or pervious. Commonly used methods include thresholding methods [18], [37], [38] and unsupervised classification methods [39], [40]. It is widely acknowledged that the selection of binary algorithms may have an influence on the accuracy of ISA extraction [38], [41]. Thus, it is necessary to explore the effectiveness of different binary methods in ISA extraction from index images.

The objective of this study is to explore the applicability of existing index-based impervious surface methods on Sentinel-2

images considering seasonal variations. We selected BCI, NBAI, CBI, and PISI, to extract ISA from images acquired during different seasons in Wuhan city, China. BCI, NBAI, and CBI were selected due to their robustness to extract urban surfaces from a complex relief when dealing with Sentinel-2 images and their capability to distinguish urban areas and backgrounds [25], [42]. Moreover, BCI index was calculated using a Gram-Schmidt orthogonalization method (BCI_GSO) and a principal component-based Procrustes analysis (BCI_PCP), respectively. Their performance on Sentinel-2 data needs more study. PISI is a more recent index that can accurately extract ISA from Landsat 8 images. Considering the efficiency and low requirements for training samples, we utilized Otsu's thresholding [43], manual thresholding, and ISODATA method to identify the impervious class. In sum, the aims of this study are to

1) systematically evaluate the performance of BCI_GSO, BCI_PCP, NBAI, CBI, and PISI indices in ISA extraction from Sentinel-2 imagery;
2) assess performances of Otsu's thresholding, manual thresholding, and ISODATA classification method for separating impervious surfaces from index images; and
3) explore the impact of seasonal variation on ISA extracted by the four index-based methods using different thresholding techniques.

II. Materials and Methodology

A. Study Area and Datasets

Located in central Hubei province, China, Wuhan city has a humid subtropical climate, characterized by abundant rainfall, sufficient heat, hot rain, hot light, cold winter, hot summer, and distinct four seasons. The Wuhan urban development zone is located in central Wuhan city (upper left longitude 113° 52′ E and latitude 30° 41′ N, lower right longitude 114° 40′ E and latitude 30° 16′N) (see Fig. 1). It is the main agglomeration area of urban functions and the key development area of urban space, covering an area of 3261 km^2, accounting for about 38.055% of the total area of Wuhan city. The administrative boundaries of towns and townships near the outer ring expressway are designated as parts of the Wuhan urban development zone. This zone consists of the core areas of seven central urban districts (i.e., Jiang'an, Jiang-han, Qiaokou, Hanyang, Wuchang, Qingshan, and Hongshan) and six suburban districts (i.e., Dongxihu, Caidian, Huangpi, Xinzhou, Jiangxia, and Hannan). It has experienced a high level of urbanization, and 80.49% of its total population are permanent urban residents in 2019 [44]. Therefore, we believe it is suitable and representative for studying the performance of different indices and seasonal impacts on index-based ISA extraction.

Sentinel-2A and 2B launched in 2015 and 2017, respectively, are twin satellites designed by the European Space Agency with the same optical sensor [45]. In this study, both Sentinel-2A and Sentinel-2B data were retrieved from January 1, 2019 to December 31, 2019. To reduce the impact of cloud cover and missing data on the extraction results of impervious surfaces, Sentinel-2 Level-1C (S2 L1C) surface reflectance data acquired with less than 10% cloud volume were selected for each season. Imagery from Sentinel-2A and Sentinel-2B was downloaded from the Sentinel Scientific Data Hub[1] (see Table I). The value

---

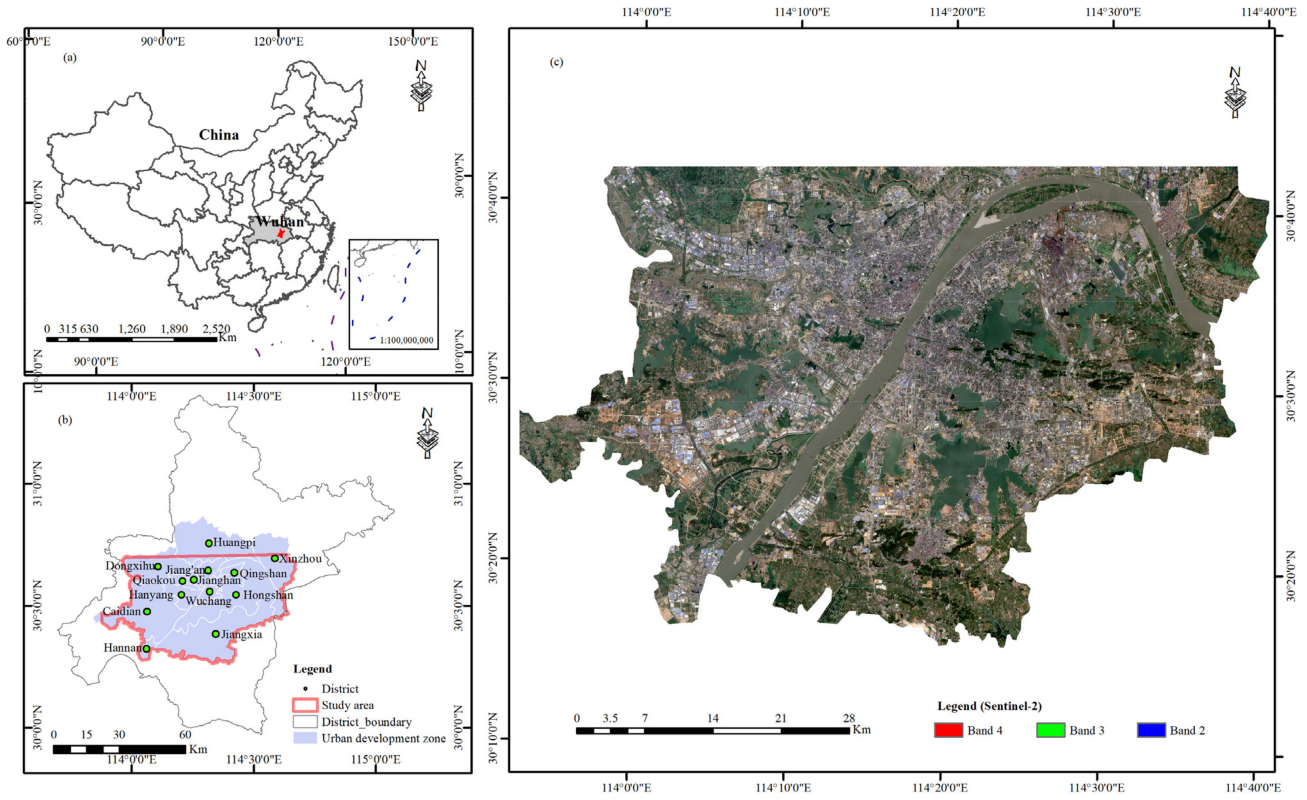[1]Freely available at https://scihub.copernicus.eu/

Fig. 1.　(a) Map of China showing the location of Wuhan city. (b) Map of Wuhan city showing the location of study area. (c) Nature composite Sentinel-2 image of study area acquired on September 22, 2019.

TABLE I
LIST OF SELECTED SENTINEL-2 IMAGES IN THE STUDY

Granule ID	Sensing date	Sensor	UTM zone	Cloud percentage
S2B_OPER_MSI_L1C_TL_EPAE_20190311T073748_A010497_T50RKU_N02.07	2019-03-11 (spring)	2B	50RKU	6.15
S2A_OPER_MSI_L1C_TL_EPAE_20190604T054120_A020621_T50RKU_N02.07	2019-06-04 (summer)	2A	50RKU	0
S2A_OPER_MSI_L1C_TL_EPAE_20190922T060638_A022194_T50RKU_N02.08	2019-09-22 (autumn)	2A	50RKU	0
S2A_MSIL1C_20191211T030121_N0208_R032_T50RKU_20191211T055310	2019-12-11 (winter)	2A	50RKU	0

of the percentage of clouds in an image can be referenced to the CLOUDY_PIXEL_PERCENTAGE field of the metadata. The downloaded Level-1C was tiled following a predefined grid of 100 × 100 km in the Universal Transverse Mercator (UTM) coordinate system based on the WGS-84 ellipsoid. Our study area corresponds to tile T50RKU.

The multispectral instrument onboard Sentinel-2 is a new type of remote sensing sensor that measures the Earth's reflected radiance in 13 spectral bands with a 10—60 m spatial resolution (see Table II), which is quite different from the spectral bands of the Landsat series. However, existing index-based ISA extraction methods were designed for images from the Landsat series. A detailed comparison between spectral bands of the two satellites was made from a radiometric perspective (see Table II) [46]. Employed bands from Sentinel-2 to calculated ISA indices can be found in Table III.

B. Image Preprocessing

The distributed S2 L1C data are ortho-image TOA (Top of Atmosphere) reflectance products, which have been geometrically and radiometrically corrected by a server-side function. To eliminate the atmospheric effect, S2 L1C images were subjected to atmospheric correction to produce Level-2A (S2 L2A) images, which are at BOA (Bop of Atmosphere) reflectance using the plug-ins sen2cor in SNAP 6.0 software. The S2 L2A product contains 12 spectral bands at varying spatial resolutions: 4 bands at 10 m (band 2, 3, 4, 8), 6 bands at 20 m (band 5, 6, 7, 8a, 11, 12), 2 bands at 60 m (band 1, 9). To make full use of all bands, S2 L2A images were resampled at spatial resolutions of 10 m using the SNAP open-source software. Since the study region was covered by a single scene, image mosaicking and geometric correction were not considered.

TABLE II
BAND NAME, SPECTRAL RANGE (NM), AND SPATIAL RESOLUTION (M) OF THE CORRESPONDING SENTINEL-2A MSI, LANDSAT-8 OLI [46]

Name	Sentinel-2A MSI		Landsat-8 OLI		
	Band (resolution/m)	Range (nm)	Band (resolution/m)	Band (resolution/m)	Range (nm)
Coastal aerosol	B1(60)	443.9±13.5	B1(60)	B1(30)	443±8
Blue	B2(10)	492.1±49	B2(10)	B2(30)	482±30
Green	B3(10)	559±23	B3(10)	B3(30)	561.5±28.5
Red	B4(10)	665±19.5	B4(10)	B4(30)	654.5±18.5
Pan				B8(15)	589.5±86.5
Red_edge1	B5(20)	703.8±10	B5(20)		
Red_edge2	B6(20)	739.1±9	B6(20)		
Red_edge3	B7(20)	779.7±14	B7(20)		
NIR_wide	B8(10)	833±66.5	B8(10)		
NIR_narrow	B8A(20)	864±16	B8A(20)	B5(30)	865±14
Water Vapor	B9(60)	943.2±13.5	B9(60)		
Cirrus	B10(60)	1376.9±38	B10(60)	B9(30)	1372±17.5
SWIR 1	B11(20)	1610.4±70.5	B11(20)	B6(30)	1608.5±42.5
SWIR 2	B12(20)	2185.7±119	B12(20)	B7(30)	2200.5±93.5

TABLE III
BANDS OF SENTINEL-2 EMPLOYED TO CALCULATE ISA INDICES

Band	Notation
B2 Blue	b_{blue}
B3 Green	b_{green}
B4 Red	b_{red}
B8A Vegetation red edge	b_{nir}
B11 SWIR1	b_{swir1}
B12 SWIR2	b_{swir2}

Data gaps caused by clouds should be considered. Many cloud detection methods for Sentinel-2 images have been developed [47], [48]. These methods can improve the quality of cloud-contaminated images in most cases. However, they require customized parameters and demand computational resources [49], [50]. In fact, S2 L1C product is distributed with associated cloud masks, including opaque cloud and cirrus cloud, which are vectors in GML format and easy to overlap with band images. Coluzzi *et al.* [51] assessed the S2 L1C cloud mask product by comparing it with reference masks and revealed the validity of the L1C product. Therefore, we performed cloud-masking on the Sentinel-2B image acquired on March 11, 2019 using the S2 L1C cloud mask product in SNAP software. After cloud masking, a 3-D gap-filling method [52] was applied to fill data gaps.

C. Impervious Surface Indices

1) Biophysical Composition Index: The BCI was proposed by Deng and Wu [23] to identify different urban biophysical compositions based on Tasseled Cap transformation (TCT). It can be calculated using the following expression:

$$\text{BCI} = \frac{(TC_1 + TC_3)/2 - TC_2}{(TC_1 + TC_3)/2 + TC_2} \quad (1)$$

where $TC_i, (i = 1, 2, 3)$ are the linearly normalized Tasseled components within the range from 0 to 1. As TCT coefficients are sensor-specific and may affect the performance of BCI, two sets of TCT coefficients were used to derive BCI index images. One was derived from Nedkov using the Gram–Schmidt orthogonalization (GSO) method [53], and the other was derived from Shi and Xu [54] using a principal component-based Procrustes analysis (PCP) method. The BCI_GSO index denotes the BCI value that was calculated using the TCT coefficients derived from the GSO method, while the BCI_PCP index denotes BCI value that was calculated using the TCT coefficients from the PCP method.

2) Normalized Built-Up Area Index (NBAI): The NBAI was designed by Waqar *et al.* [30] to extract bare soil and built-up area from Landsat imagery and can be computed as follows:

$$\text{NBAI} = \frac{b_{swir2} - b_{swir1}/b_{green}}{b_{swir2} + b_{swir1}/b_{green}} \quad (2)$$

where b_{swir1} and b_{swir2} are two SWIR bands, satisfying $b_{swir2} > b_{swir1}$, and b_{green} denotes the reflectance of the Green band.

3) Combinational Build-Up Index (CBI): The CBI [33] takes advantage of three indices to map ISA: the first component produced by principal component analysis (PC_1), normalized difference water index (NDWI) [55], and soil-adjusted vegetation index (SAVI) [56]. It can be computed as follows:

$$\text{CBI} = \frac{(PC_1 + NDWI)/2 - SAVI}{(PC_1 + NDWI)/2 + SAVI} \quad (3)$$

where PC_1, NDWI, and SAVI are linearly normalized to a range [0, 1].

TABLE IV
DETAILS FOR THE SELECTED ISA EXTRACTION INDICES

Index	Study area	Sensors	Water mask	Value range
BCI [23] [a]	Grafton, USA Wisconsin, USA	Landsat ETM+, IKONOS, MODIS	Y	[-1,1]
NBAI [30]	Islamabad, Pakistan	Landsat TM	Y	[-1,1]
CBI [33]	Qingdao, China Okinawa, Japan Fushun, China Berlin, Germany Wuhan, China	Landsat-8 OLI WorldView-2 SPOT-5 HyMap	Y	[-1,1]
PISI [25]	Guangzhou, China Shenyang, China Xining, China	Landsat 8 OLI	Y	[-1,1]

[a]BCI we used were BCI_GSO and BCI_PCP, BCI_GSO denoted the BCI index that was calculated using the TCT coefficients derived from the GSO method, while BCI_PCP denoted the BCI index that was calculated using the TCT coefficients derived from the PCP method.

The NDWI and SAVI are calculated as follows:

$$NDWI = \frac{b_{green} - b_{nir}}{b_{green} + b_{nir}} \qquad (4)$$

$$SAVI = \frac{(b_{red} - b_{nir})(1 + L)}{(b_{red} + b_{nir} + L)} \qquad (5)$$

where L is a correction factor, set to 0.5 in this study.

4) Perpendicular Impervious Surface Index (PISI): The PISI [25] was developed to extract ISA from Landsat 8 OLI images. The formula for PISI can be expressed as follows:

$$\text{PISI} = 0.8192 b_{blue} - 0.5735 b_{nir} + 0.075 \qquad (6)$$

where b_{blue} and b_{nir} denote the reflectance of the Blue and NIR band, respectively.

Table IV presents the details for the selected ISA extraction indices. Note that

1) all of these selected indices are applicable to medium-resolution images (Landsat), but their suitability for high-resolution images should be examined except for BCI and CBI;
2) the values of ISA indices all range from −1 to +1;
3) water bodies need to be masked out from images before using these indices to acquire ISA. NDWI and MNDWI [57] are two commonly used water extraction indices.

NDWI is considered a more effective way to extract water bodies when using Sentinel-2 data [41], [58]. Therefore, NDWI was applied, and a default value of 0 was set to mask out water bodies in this work.

D. Mapping Impervious Surface

Thresholding and unsupervised classification methods were implemented over these images to separate ISA from non-ISA after calculating the index image according to the equations previously discussed in this section. The binary methods used in this study were Otsu's automatic thresholding method, manual thresholding, and ISODATA classification method. All were executed in ENVI 5.3 software.

1) Thresholding Method: Manual thresholding requires expertise when defining a suitable threshold, usually via a trial and error process; an alternative is an automatic thresholding. As the most commonly used automatic thresholding method, Otsu's thresholding [43] has been successfully implemented to extract land covers from satellite index images, including ISA [25], [36], built-up land features [59], water body [60], and shadows [61]. The purpose of Otsu's method is to find a value that minimizes the intraclass variance while maximizes interclass variance.

2) ISODATA Classification Method: ISODATA is an unsupervised classification algorithm that has also been successfully applied to classify grayscale images into ISA and non-ISA classes [39], [40]. We used ISODATA to classify the index images into several clusters and merge the derived clusters into pervious and impervious surfaces. In this study, we compared the performances of Otsu's thresholding method, manual thresholding, and ISODATA classification method on Sentinel-2 index images for ISA extraction.

III. RESULTS

A. Thresholds of Index Images

The ISAs were extracted for the study area from Sentinel-2 images collected over different seasons by applying NBAI, PISI, BCI_GSO, BCI_PCP, and CBI indexes. Otsu's thresholding method was implemented on the index images in the ENVI 5.3 IDL programming environment. The manual thresholding was selected via a trial-and-error process. To improve efficiency, we used the threshold from Otsu's method as an initial value and manually adjusted the threshold. Histograms of each index image over different seasons are shown in Fig. 2. The derived thresholds are presented in Table V.

As illustrated in Table V, optimal thresholds selected for PISI, BCI_PCP, and CBI index images using Otsu's method were close to those values determined manually. For BCI_GSO and NBAI index images, however, numerical differences became larger, indicating that Otsu's thresholding method is not always superior to manual thresholding.

B. Results of ISA Extraction

1) ISA Extraction Using the Thresholding Method: The PISI, BCI_GSO, BCI_PCP, CBI, and NBAI index images were reclassified into pervious and impervious classes using the selected thresholds shown in Table V. The ISA extraction results using Otsu's method and manual thresholding can be found in Figs. 3 and 4, respectively.

In general, the manual thresholding method was more reliable for ISA extraction from the five seasonal index images. Otsu's method achieved satisfactory results from PISI and CBI index images but failed to present decent extraction results from BCI_GSO and NBAI index images collected over four seasons. For BCI_PCP index images, Otsu's method was effective except during the winter season.

To explain the reason for this phenomenon, we analyzed the distribution of gray values in each index image. We noticed that the performance of Otsu's method was highly related to the histogram of the image. When the histogram of the image presented a two-peaked pattern, Otsu's method successfully segmented the
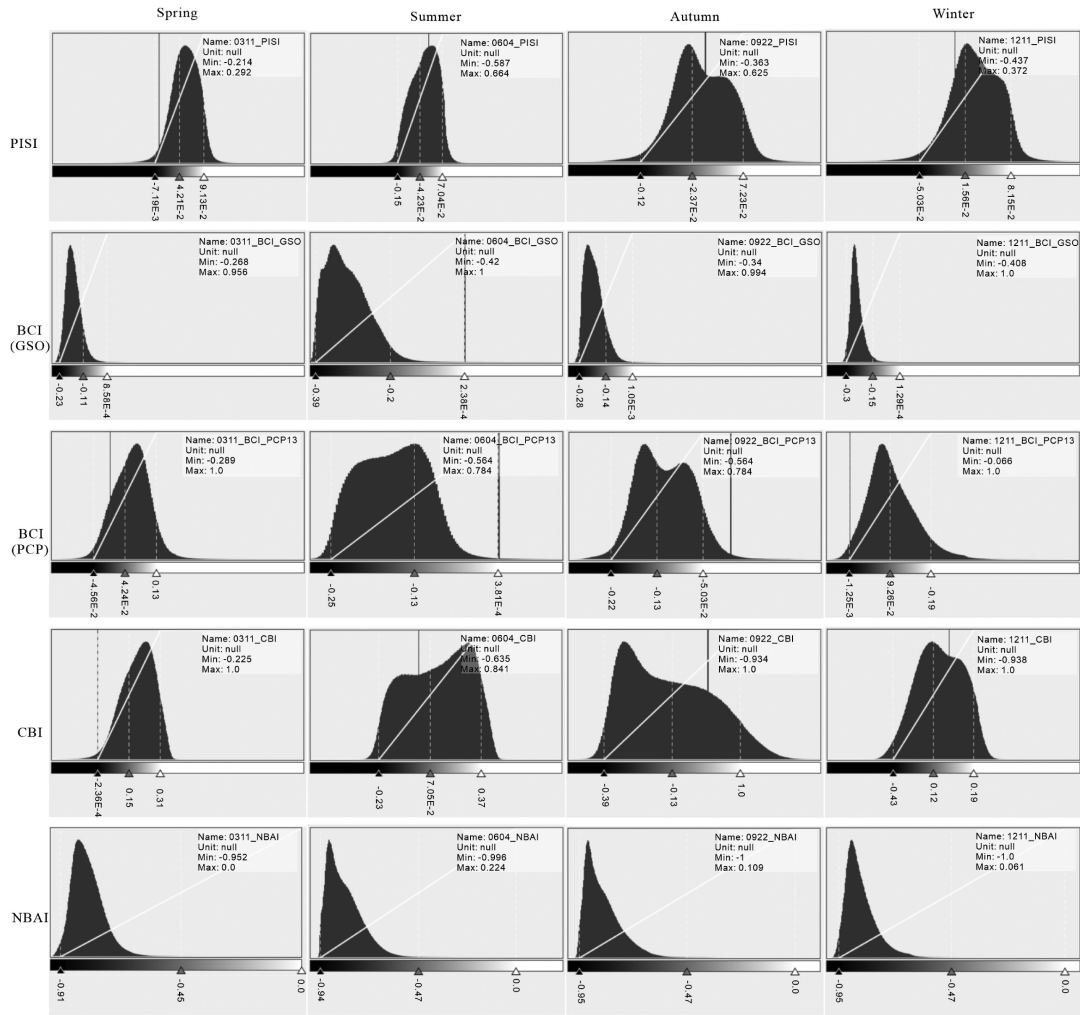
Fig. 2. Histograms of ISA index images over four seasons.

TABLE V
OPTIMAL THRESHOLDS BASED ON OTSU'S ALGORITHM AND MANUAL PROCESS FOR DIFFERENT SEASONAL IMAGES

Index image	Spring		Summer		Autumn		Winter	
	Otsu	Manual	Otsu	Manual	Otsu	Manual	Otsu	Manual
PISI	0.0314	0.0560	-0.0390	-0.0050	-0.0224	0	0.0169	0.0300
BCI_GSO	-0.084	-0.170	-0.1573	-0.3019	-0.1047	-0.2050	-0.1212	-0.2500
BCI_PCP	0.0340	0.049	-0.1515	-0.1515	-0.1168	-0.1168	0.0465	0.085
CBI	0.0890	0.2000	0.0810	0.1700	-0.1361	-0.1300	-0.1094	-0.0500
NBAI	-0.4031	-0.8080	-0.4167	-0.8300	-0.4260	-0.8500	-0.4300	-0.8650

image. Our findings coincided with other studies that pointed out that Otsu's method could fail to select optimal thresholds when the histogram of the image was unimodal or close to unimodal [62], [63]. As shown in Fig. 2, histograms of PISI index images in summer, autumn, and winter, the BCI_PCP index images in summer and autumn, and the CBI index images in summer, autumn, and winter were bimodal or close to bimodal. Although the PISI, BCI_PCP, and CBI index images in the spring were not bimodal, their gray values were evenly distributed, thus satisfactory results were achieved. For BCI_GSO and NBAI

index images in the four seasons and BCI_PCP index images in winter, their gray value distribution patterns were unimodal or close to unimodal.

Comparing Figs. 3 and 4, we observed that Otsu's method had an issue of overestimating ISA in PISI index images while underestimating ISA in all seasons. This was presumably due to the fact that the PISI index was sensitive to water, leading to confusion, to a certain extent, between urban areas and bare soil. These types of land cover had higher gray values and were classified as the impervious class using Otsu's method. Otsu's
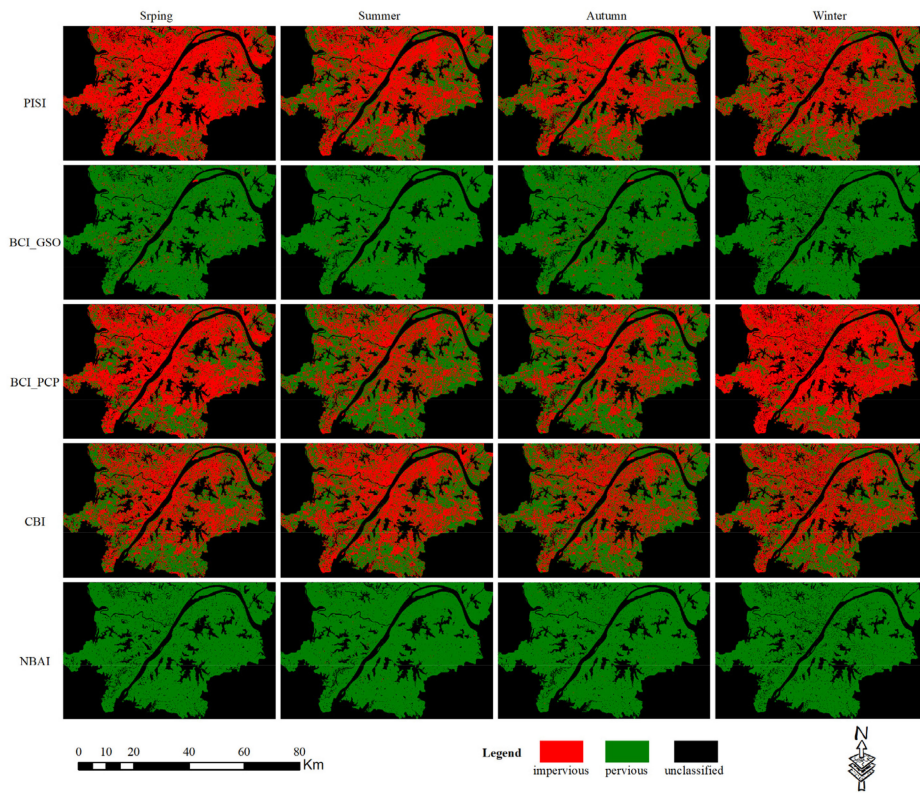
Fig. 3. Impervious surface extracted using Otsu's method from PISI, BCI_GSO, BCI_PCP, CBI, and NBAI index images.
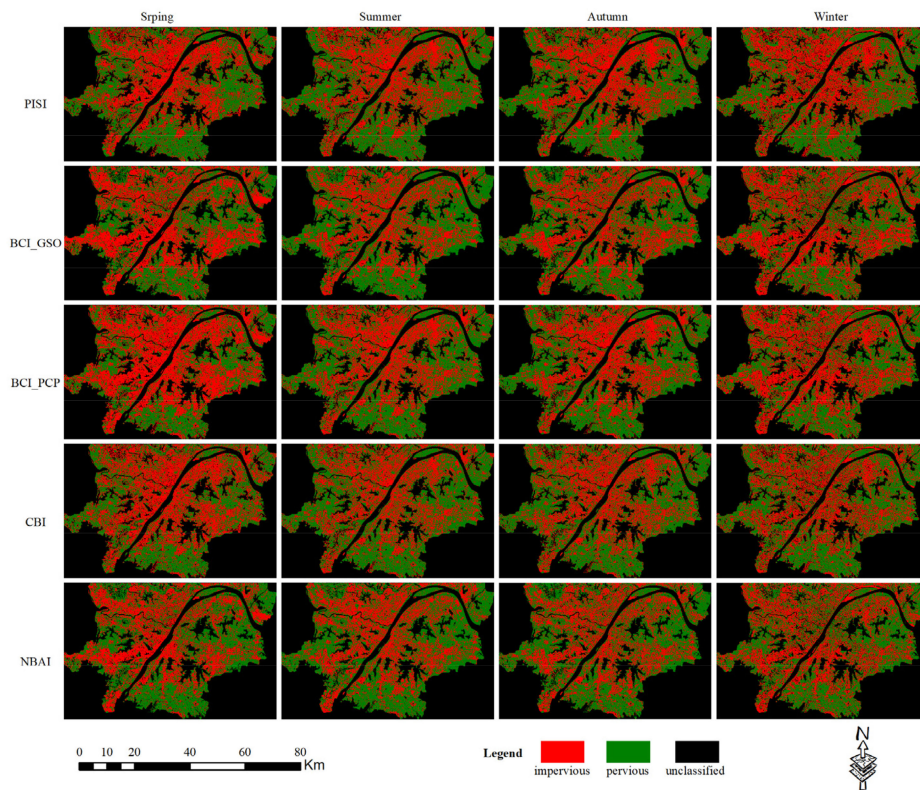
Fig. 4. Impervious surface extracted using manual thresholding from PISI, BCI_GSO, BCI_PCP, CBI, and NBAI index images.
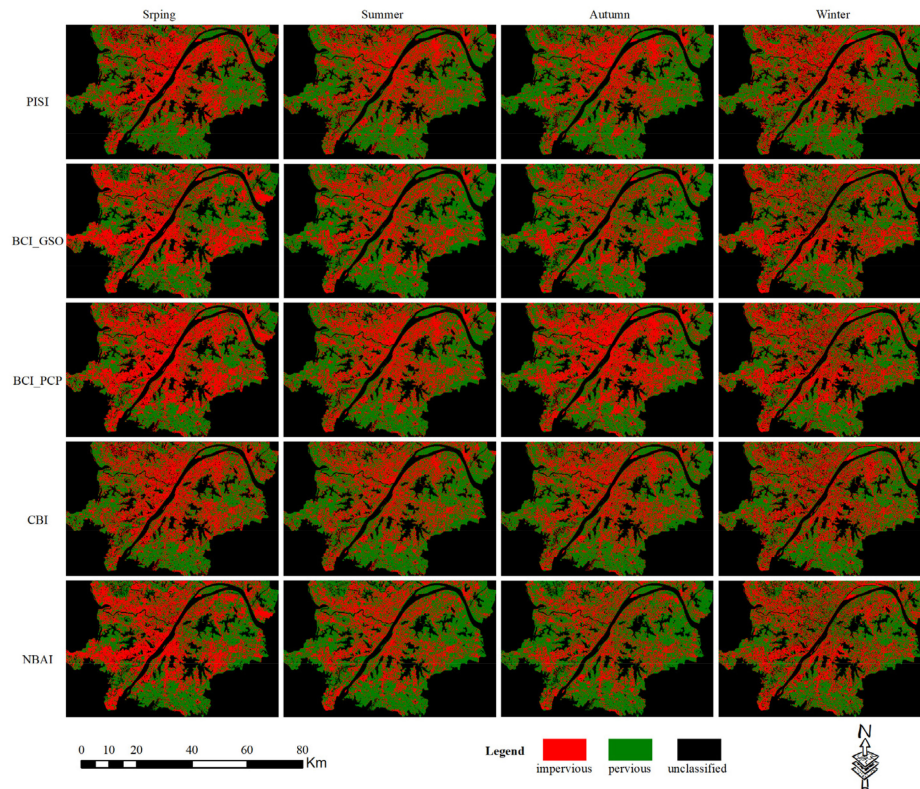
Fig. 5. Impervious surface extracted using ISODATA classification method from PISI, BCI_GSO, BCI_PCP, CBI, and NBAI index images.

method failed to select the optimal threshold for BCI_GSO and NBAI. Using the derived threshold, massive impervious surfaces were segmented and wrongly classified as pervious surfaces. In this case, Otsu's method underestimated ISA in BCI and NBAI index images. Moreover, ISA overestimated from BCI_PCP index image, especially in winter, a dry season in Wuhan city. Under this circumstance, it was more challenging to distinguish between bare soil and impervious surface [42].

2) ISA Extraction Using ISODATA Method: ISODATA method extracted the ISA based on classification. First, index images were classified into nine clusters. In this algorithm, parameters of min and max numbers were set to 7 and 12, respectively, and default values were used for other parameters. After the classification, derived clusters were combined into pervious and impervious classes with the help of high-resolution Google Earth images.

Comparing Figs. 5, 3, and 4, we could conclude that, among the three ISA extraction methods for all index images, Otsu's method performed the worst, while ISODATA and manual thresholding were similar and outperformed the Otsu's method.

To better understand how impervious surface categories and seasons impact the ISA classification via different indices, we selected six typical impervious surface categories for analysis. Referring to [34] and considering the geographical environment and industrial structure of Wuhan, these six categories of impervious surfaces include island areas, road infrastructure, residential areas, urban–rural junctions, central business districts (CBDs), and industrial areas. Fig. 6 presents the results of ISA extraction for these categories of impervious surfaces. To

better compare and illustrate the extraction results, images were segmented and classified using eCognition software. The classification results were manually modified further with the help of high-resolution Google Earth images. These results served as ground-truthing data.

Tianxingzhou Island [see Fig. 6(a)], lying in the center of the Yangtze River and covered by farmlands, was formed by the natural alluvial deposits. It is clear that seasonal fluctuations of the river influenced the ISA extraction results. ISA was overestimated in all seasons, except for summer. The reason for this is that water levels of the Yangtze River are relatively high in summer, leading to the rapid movement of sediments and less sediment accumulation. In addition, it was observed that all indices were sensitive to water and confused ISA with bare land.

Fig. 6(b) shows the extraction results for road infrastructure (e.g., highways), one accurately classified category of urban impervious surfaces. In winter, with low vegetation coverage, the linear features of highways were extracted in a complete manner. PISI and BCI_PCP outperformed the other indices and were the closest to the ground truth. The NBAI, CBI, and BCI_GSO results were subject to seasonal dynamics. The failure of these three indices also indicated their inability to distinguish ISA from other land cover types.

Residential areas [see Fig. 6(c)], including a variety of land cover types, such as high buildings, highways, vegetation, water, shadows, etc., are located along the East Lake. Due to the green urban management, Wuhan city in all four seasons is largely covered by vegetation. The PISI, BCI_PCP, and CBI results
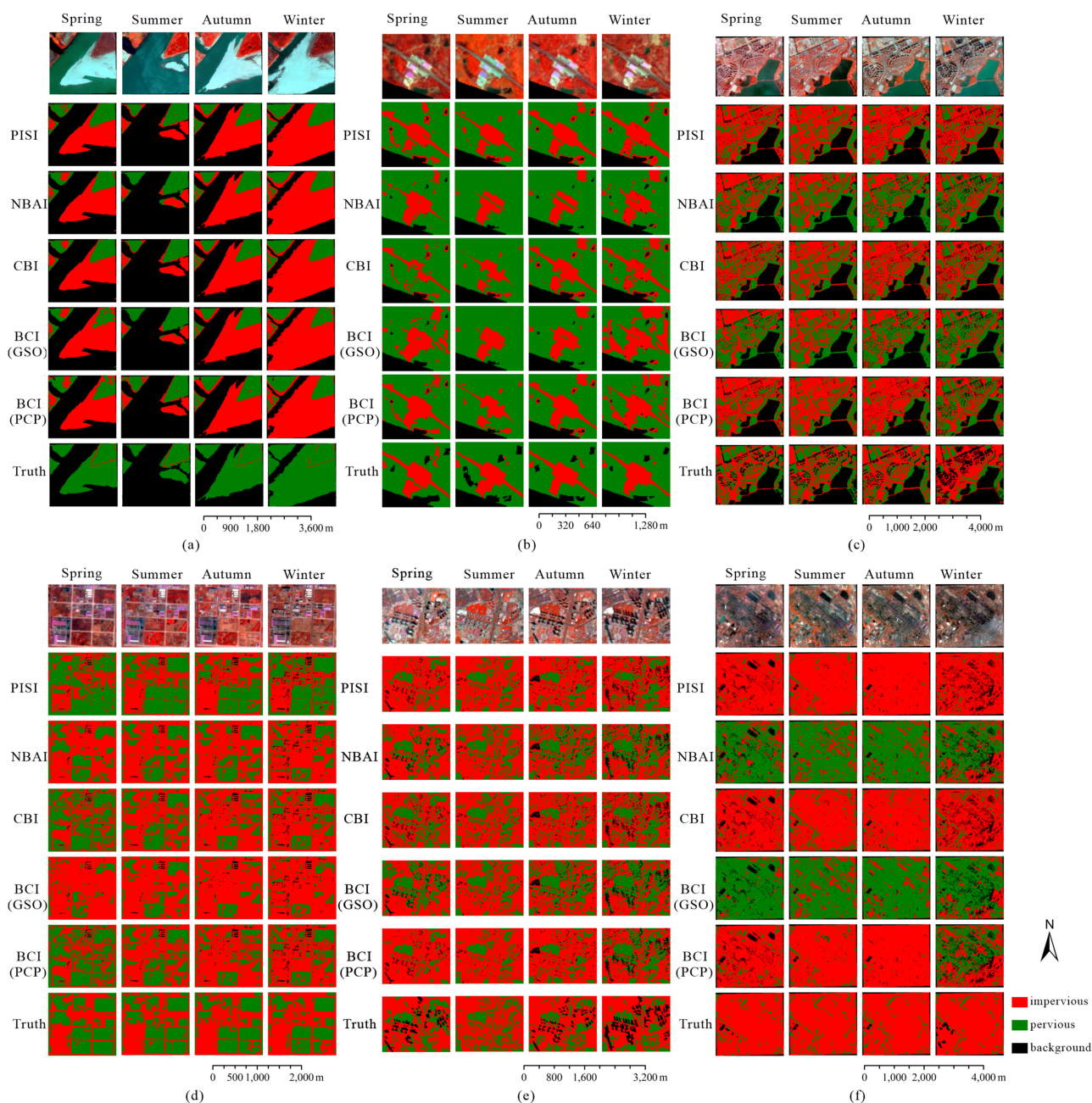
Fig. 6.   ISA distribution extracted by PISI, NBAI, CBI, BCI_GSO, and BCI_PCP index-based method from four seasonal Sentinel-2 images in the six subsets of the study area: island (a); expressway (b); residential area (c); urban-rural junctions (d); CBD (e); industrial area(f). From top to bottom rows, they are subsets of the original Sentinel-2 images (pseudo-colors), ISA distribution extracted by PISI, NBAI, CBI, BCI_GSO, and BCI_PCP indices, and truth data, respectively. From left to right columns, they are pseudo-color images in spring, summer, autumn, and winter, respectively.

retained more detailed information about impervious surfaces (such as roads and buildings), but were sensitive to water bodies and shadows. NBAI and BCI_GSO, however, were able to distinguish impervious surfaces from water bodies.

Urban–rural junctions [see Fig. 6(d)] are located in Wuhan East Lake High-tech Development Zone, which is a representative urban expansion area with distinct seasonal variations in vegetation coverage. Compared with the other four indices, we found that PISI was more stable to seasonal changes in vegetation and effectively separated impervious surfaces from

bare soil. CBI and BCI_PCP could extract ISA accurately from most images in winter with a slight improvement over the other two indices, but BCI_GSO overestimated ISA because of its inability to accurately distinguish impervious surfaces from bare soil.

CBDs [see Fig. 6(e)], with dominant land covers of high buildings, roads, vegetation, and shadows, are located in Hankou. Similar to residential areas, certain areas of the CBDs were covered with vegetation throughout the year. CBDs, however, are characterized by the shadows cast by high-rise buildings.

We found that PISI and BCI_PCP retained more details from buildings and roads from all images. Roads extracted by NBAI, CBI, and BCI_GSO in summer and autumn were more accurate. In these two seasons, bare soil was covered by vigorous vegetation, causing less confusion between bare soil and urban areas.

Industrial areas [see Fig. 6(f)] belonging to Wuhan Iron and Steel (Group) Company are located in the Qingshan District, Wuhan. As compared to residential areas, buildings in industrial areas are denser with limited seasonal changes. We found that the PISI and CBI performed effectively in extracting impervious surfaces with a dark tone, but the NBAI and BCI_GSO generally underestimated impervious surfaces. BCI_PCP worked effectively, with the exception of the winter season.

C. Accuracy Assessment

To quantitatively evaluate the accuracy of the five impervious surface indices for each seasonal image, we selected a total of 200 samples of the impervious (100 samples) and pervious class (100 samples). Selected samples were used to derive the confusion matrix, overall accuracy (OA), and Kappa as assessment indicators. Table VI presents the accuracy assessment.

We found that the selection of binary methods played a role in the accuracy of ISA extraction. Otsu's method obtained satisfactory results in PISI, BCI_PCP, and CBI index images but failed to accurately extract ISAs from BCI_GSO and NBAI index images collected over four seasons, with an average OA of 46.22% and 35.37%, Kappa of 0.075 and 0.0103, respectively.

The ISODATA method generally outperformed Otsu's method in extracting ISAs and achieved an accuracy as high as the manual method for all index images collected over different seasons. In this case, the performance of the five tested indices on multiseasonal Sentinel-2 images was compared using the results extracted by ISODATA. As shown in Table VI, we observed that the PISI index (with an average OA of 92.64% and Kappa of 0.84) could estimate the impervious surface more accurately than the other four indices, while the results extracted from the CBI index (with an average OA of 75.69% and Kappa of 0.52) were the least effective. The accuracy of ISA extraction using the NBAI (with an average OA of 88.12% and Kappa of 0.73) was slightly lower than that using PISI index. The TCT coefficients, however, may affect the accuracy of BCI. The BCI index had an average OA of 86.37% and Kappa of 0.69 when this index was calculated using the parameters derived from the Gram–Schmidt orthogonalization method (i.e., BCI_GSO). The performance of the BCI index was improved with an average OA of 88.41% and Kappa of 0.76 when this index was calculated using parameters derived from the principle component-based Procrusters analysis (i.e., BCI_PCP).

For each impervious surface index, the accuracy of ISA extraction based on the three selected methods showed seasonal variations. The accuracy of extracted impervious surfaces in summer was generally the highest, while the accuracy of extracted impervious surfaces in winter was the lowest.

D. Statistics of Extracted ISA in the Study Area

Since the ISODATA method delivered the most accurate results for the impervious surface in the index images, we counted

TABLE VI
ACCURACY ASSESSMENT RESULTS OF DIFFERENT ISA EXTRACTION METHODS

ISA Indices	Accuracy Measures	Spring	Summer	Autumn	Winter	Average
		ISODATA classification method				
PISI	OA (%)	93.79	94.91	91.07	90.80	92.64
	Kappa	0.8615	0.8867	0.8077	0.808	0.8410
BCI_GSO	OA (%)	81.75	92.94	88.05	82.73	86.37
	Kappa	0.5614	0.8431	0.7418	0.6261	0.6931
BCI_PCP	OA (%)	86.71	92.75	89.62	84.55	88.41
	Kappa	0.7210	0.8356	0.7857	0.6867	0.7573
CBI	OA (%)	67.85	80.92	74.77	79.22	75.69
	Kappa	0.3919	0.6107	0.5038	0.5889	0.5238
NBAI	OA (%)	87.17	92.15	87.03	85.72	88.02
	Kappa	0.7007	0.8248	0.7195	0.6937	0.7347
		Otsu's method				
PISI	OA (%)	81.24	94.33	89.28	87.09	87.99
	Kappa	0.5087	0.8714	0.7644	0.7213	0.7165
BCI_GSO	OA (%)	52.62	39.28	55.64	38.15	46.22
	Kappa	0.2045	0.0436	0.2547	0.053	0.1390
BCI_PCP	OA (%)	78.25	92.07	89.14	67.19	81.66
	Kappa	0.5263	0.8213	0.7775	0.2874	0.6031
CBI	OA (%)	67.65	87.64	75.71	81.54	78.14
	Kappa	0.3808	0.7331	0.518	0.6229	0.5637
NBAI	OA (%)	35.37	35.37	35.37	35.37	35.37
	Kappa	0.0018	0	0.0166	0.0226	0.0103
		By manual				
PISI	OA (%)	93.72	94.90	91.38	89.84	92.46
	Kappa	0.8597	0.8863	0.815	0.7856	0.8367
BCI_GSO	OA (%)	82.79	93.01	88.05	81.89	86.44
	Kappa	0.5933	0.8444	0.7418	0.6038	0.6958
BCI_PCP	OA (%)	84.71	92.72	89.14	82.21	87.20
	Kappa	0.6760	0.8348	0.7775	0.6363	0.7312
CBI	OA (%)	67.54	81.78	75.19	79.13	75.91
	Kappa	0.3992	0.6258	0.51	0.5873	0.5306
NBAI	OA (%)	89.21	92.75	87.03	85.81	88.70
	Kappa	0.7534	0.8366	0.7184	0.6959	0.7511

the impervious surface results based on the ISODATA method, as shown in Table VII. We can draw the following conclusions.
1) In general, the proportion of ISA extracted from the four index images presented a slow upward trend from summer to winter.
2) The percentage of impervious surfaces extracted in summer was generally the lowest, presumably due to the vigorous growth of vegetation in summer, resulting in massively obscured ISA.
3) Estimations of ISA using BCI_GSO, CBI, and NBAI were more subject to seasonal changes compared to results using PISI and BCI_PCP.

IV. DISCUSSION

In this article, we compared and analyzed the performance of PISI, BCI_GSO, BCI_PCP, CBI, and NBAI on ISA extraction from Sentinel-2 images and explored the impact of seasonality on ISA extraction results. Different from [38], this article focuses on evaluating the applicability of these indices on Sentinel-2 images and their sensitivity to seasonal change. Moreover, the performance of these indices may be influenced by choice of

TABLE VII
QUANTIFICATION OF LAND COVER (%) IN THE STUDY AREA

Method	Spring		Summer		Autumn		Winter		variance	
	ISA	pervious	ISA	pervious	ISA	pervious	ISA	pervious	ISA	pervious
PISI	38.44	43.77	36.20	48.34	39.30	44.25	37.30	45.45	1.3673	3.153619
BCI_GSO	36.79	45.43	34.22	50.32	33.40	50.16	40.33	42.43	7.291125	11.08223
BCI_PCP	38.90	45.64	37.37	38.86	37.37	39.95	40.55	42.95	1.726819	7.03105
CBI	40.16	42.06	34.70	49.84	35.83	47.72	37.66	45.09	4.262369	8.482419
NBAI	40.65	41.56	32.69	51.85	34.28	49.28	37.93	44.82	9.665319	15.75172

binary methods. In this study, we explored the performance of Otsu's thresholding, manual thresholding, and ISODATA classification method in depth. A quantitative accuracy assessment indicates that the PISI outperformed the other tested methods in identifying impervious surfaces with the least sensitivity to seasonal changes. In addition, the ISODATA method can reliably extract ISA from multiseasonal Sentinel-2 index images, regardless of data distribution.

Our findings on the performance of five selected indices on ISA extraction are comparable to previous studies [25]. PISI outperforms the other four indices, especially with the extensive existence of bare soil. ISODATA classification method takes advantage of the features to extract binary ISA results, regardless of the grayscale distribution of index images. Seasonal variations, nevertheless, may have impacts on the accuracy and proportion of extracted ISAs. Experimental results show that BCI_GSO, BCI_PCP, and NBAI are largely sensitive to seasonal changes, while PISI and CBI are relatively robust to seasonality when extracting ISAs from different images. Images acquired in different seasons tend to present varying data distribution patterns. When distribution patterns obey a bimodal pattern (or close to a bimodal pattern), Otsu's method can effectively separate ISA from non-ISA. However, under other distribution patterns, the performance of Otsu's method is not satisfactory. In addition, the proportion of extracted ISA in the study area differs across the seasons due to discrepancies in land use patterns. In general, ISA tends to be underestimated in early summer and autumn, while overestimated in spring and winter.

Although estimating the ISA based on spectral indices has achieved promising results, challenges in extracting ISA from Sentinel-2 images still remain. First, the spectral similarity between different land covers poses great difficulty in ISA extraction. In areas with barely any vegetation coverage, it is difficult to distinguish impervious surfaces from bare soil. Therefore, Sentinel-2 images acquired during the summer season are recommended for ISA mapping. Second, ISA indices are sensitive to seasons, and seasonal changes can lead to discrepancies in the quantitative estimation of impervious surfaces. Future studies should explore the possibility of designing seasonal-robust indices. In addition, shadow issues inherent to the Sentinel-2 image also might affect the accuracy of ISA mapping.

In this study, we paid less attention to building shadows, given the fact that such an issue occurs mainly in high-resolution or super-high-resolution images [64]–[66]. However, we noticed that building shadows affected the quality of ISA extracted from Sentinel-2 images. As shown in Fig. 6(c), (e), and (f), building shadows can be identified in these well-developed urban areas, potentially causing difficulties for classification

algorithms. Moreover, the spectrum of building shadows and low albedo features are similar to that of water. They can be mistakenly classified as water when using NDWI. A possible solution to improve the accuracy of ISA results would be to develop a new building shadow detection method, making full use of the rich spectral information in Sentinel-2 images, aiming to separate these spectrally similar features before the ISA extraction procedure.

V. CONCLUSION

Freely available Sentinel-2 data offer new opportunities for large area impervious surface mapping. This study marks the first attempt to assess the performances of different spectral indices for ISA extraction using multiseasonal Sentinel-2 images. Five index-based impervious surface methods (PISI, BCI_GSO, BCI_PCP, CBI, and NBAI) and three impervious surface binary methods (manual thresholding method, Otsu's thresholding method, and ISODATA classification method) were tested on multiseasonal Sentinel-2 images in the main urban area of Wuhan, China. We used OA and kappa values as assessment indicators to evaluate the results. Moreover, we investigated the performance of these methods in six different types of impervious surfaces.

Conclusions can be reached as follows:
1) Existing index-based impervious surface extraction methods designed primarily for Landsat images have certain adaptability to multiseasonal Sentinel-2 images.
2) PISI has the greatest capability to discriminate impervious surfaces from nonimpervious surfaces in Sentinel-2 images as compared to the other four indices.
3) The choice of binary methods has an influence on ISA estimation results. ISODATA classification method and manual thresholding have similar results when generating ISA maps, while Otsu's method fails to achieve stable ISA mapping.
4) Seasonal variations affect the performance of different ISA indices as well as the general extension of estimated ISA in the study area. PISI is relatively robust to the seasonal variations. The results further reveal that summer is the best season to map ISA from Sentinel-2 images.

This study provides a reference for the selection of spectral indices for ISA extraction from Sentinel-2 images in relation to seasonal variations and the selection of an appropriate binary processing method. This research contributes to the further study and application of Sentinel-2 data. In future work, we plan to focus on developing a seasonal robust ISA index for Sentinel-2 images.

References

[1] Q. Weng, "Remote sensing of impervious surfaces in the urban areas: Requirements, methods, and trends," *Remote Sens. Environ.*, vol. 117, pp. 34–49, 2012.

[2] X. Cao, X. Gao, Z. Shen, and R. Li, "Expansion of urban impervious surfaces in Xining city based on GEE and Landsat time series data," *IEEE Access*, vol. 8, pp. 147097–147111, Aug. 2020, doi: 10.1109/ACCESS.2020.3013640.

[3] F. Yuan and M. E. Bauer, "Comparison of impervious surface area and normalized difference vegetation index as indicators of surface urban heat island effects in Landsat imagery," *Remote Sens. Environ.*, vol. 106, pp. 375–386, 2007.

[4] M. K. Firozjaei *et al.*, "Evaluating the spectral indices efficiency to quantify daytime surface anthropogenic heat island intensity: An intercontinental methodology," *Remote Sens,* vol. 12, no. 23, 2020, Art. no. 2854.

[5] N. Yao *et al.*, "Combined effects of impervious surface change and large-scale afforestation on the surface urban heat island intensity of Beijing, China, based on remote sensing analysis," *Remote Sens*, vol. 12, no. 22, 2020, Art. no. 3906.

[6] H. Yu, Y. Zhao, and Y. Fu, "Optimization of impervious surface space layout for prevention of urban rainstorm waterlogging: A case study of Guangzhou, China," *Int. J. Environ. Res. Public Health*, vol. 16, 2019, Art. no. 3613.

[7] L. Zhang, M. Zhang, and Y. Yao, "Mapping seasonal impervious surface dynamics in Wuhan urban agglomeration, China from 2000 to 2016," *Int. J. Appl. Earth Observ. Geoinf.*, vol. 70, pp. 51–61, 2018.

[8] Z. Shao and C. Liu, "The integrated use of DMSP-OLS nighttime light and MODIS data for monitoring large-scale impervious surface dynamics: A case study in the Yangtze river delta," *Remote Sens,* vol. 6, pp. 9359–9378, 2014.

[9] L. Zhang, Q. Weng, and Z. Shao, "An evaluation of monthly impervious surface dynamics by fusing Landsat and MODIS time series in the Pearl river delta, China, from 2000 to 2015," *Remote Sens. Environ.*, vol. 201, pp. 99–114, 2017.

[10] X. Song *et al.*, "Characterizing the magnitude, timing and duration of urban growth from time series of Landsat-based estimates of impervious cover," *Remote Sens. Environ.*, vol. 175, pp. 1–13, 2016.

[11] M. Misra, D. Kumar, and S. Shekhar, "Assessing machine learning based supervised classifiers for built-up impervious surface area extraction from Sentinel-2 images," *Urban Forestry Urban Green.*, vol. 53, no. 14, 2020, Art. no. 126714.

[12] R. Xu, J. Liu, and J. Xu, "Extraction of high-precision urban impervious surfaces from Sentinel-2 multispectral imagery via modified linear spectral mixture analysis," *Sensors*, vol. 18, 2018, Art. no. 2873.

[13] M. E. Cablk and T. B. Minor, "Detecting and discriminating impervious cover with high-resolution IKONOS data using principal component analysis and morphological operators," *Int. J. Remote Sens.*, vol. 24, pp. 4627–4645, 2003.

[14] D. Lu and Q. Weng, "Extraction of urban impervious surfaces from an IKONOS image," *Int. J. Remote Sens.*, vol. 30, pp. 1297–1311, 2009.

[15] C. Gómez, J. C. White, and M. A. Wulder, "Optical remotely sensed time series data for land cover classification: A review," *J. Photogramm. Remote Sens.*, vol. 116, pp. 55–72, 2016.

[16] T. Slonecker, L. Milheim, and P. Claggett, "Landscape indicators and land cover change in the mid-Atlantic region of the United States, 1973-2001," *GISci. Remote Sens.*, vol. 47, pp. 163–186, 2010.

[17] G. Xian, H. Shi, J. Dewitz, and Z. Wu, "Performances of Worldview 3, Sentinel 2, and Landsat 8 data in mapping impervious surface," *Remote Sens. Appl., Soc. Environ.*, vol. 15, 2019, Art. no. 100246.

[18] S. I. Deliry, Z. Y. Avdan, and U. Avdan, "Extracting urban impervious surfaces from Sentinel-2 and Landsat-8 satellite data for urban planning and environmental management," *Environ. Sci. Pollut. Res.*, vol. 28, pp. 6572–6586, 2021.

[19] X. Hu and Q. Weng, "Estimating impervious surfaces from medium spatial resolution imagery using the self-organizing map and multi-layer perceptron neural networks," *Remote Sens. Environ.*, vol. 113, pp. 2089–2102, 2009.

[20] L. Shi *et al.*, "Impervious surface change mapping with an uncertainty-based spatial-temporal consistency model: A case study in Wuhan city using Landsat time-series datasets from 1987 to 2016," *Remote Sens.,* vol. 9, no. 19, 2017, Art. no. 1148.

[21] C. Deng and C. Wu, "A spatially adaptive spectral mixture analysis for mapping subpixel urban impervious surface distribution," *Remote Sens. Environ.*, vol. 133, pp. 62–70, 2013.

[22] F. Yang, B. Matsushita, T. Fukushima, and W. Yang, "Temporal mixture analysis for estimating impervious surface area from multi-temporal MODIS NDVI data in Japan," *J. Photogramm. Remote Sens.*, vol. 72, pp. 90–98, 2012.

[23] C. Deng and C. Wu, "BCI: A biophysical composition index for remote sensing of urban environments," *Remote Sens. Environ.*, vol. 127, pp. 247–259, 2012.

[24] C. Liu, Z. Shao, M. Chen, and H. Luo, "MNDISI: A multi-source composition index for impervious surface area estimation at the individual city scale," *Remote Sens. Lett.*, vol. 4, pp. 803–812, 2013.

[25] Y. Tian, H. Chen, Q. Song, and K. Zheng, "A novel index for impervious surface area mapping: Development and validation," *Remote Sens.,* vol. 10, 2018, Art. no. 1521.

[26] H. Xu, "Analysis of impervious surface and its impact on urban heat environment using the normalized difference impervious surface index," *Photogramm. Eng. Remote Sens.*, vol. 76, pp. 557–565, 2010.

[27] Y. Zha, J. Gao, and S. Ni, "Use of normalized difference built-up index in automatically mapping urban areas from TM imagery," *Int. J. Remote Sens.*, vol. 24, pp. 583–594, Feb. 2003.

[28] H. Xu, "A new index for delineating built-up land features in satellite imagery," *Int. J. Remote Sens.*, vol. 29, pp. 4269–4276, 2008.

[29] J. Chen *et al.*, "Extract residential areas automatically by new built-up index," in *Proc. 18th Int. Conf. Geoinf.*, Beijing, China, 2010, pp. 1–5, doi: 10.1109/GEOINFORMATICS.2010.5567823.

[30] M. M. Waqar, J. F. Mirza, R. Mumtaz, and E. Hussain, "Development of new indices for extraction of built-up area & bare soil from Landsat data," *Open Access Sci. Rep.*, vol. 1, pp. 2–4, 2012.

[31] Y. Liu *et al.*, "Spatiotemporal dynamics of the urban sprawl in a typical urban agglomeration: A case study on Southern Jiangsu, China (1983–2007)," *Front. Earth Sci.*, vol. 8, pp. 490–504, 2014.

[32] Z. Wang, C. Gang, X. Li, Y. Chen, and J. Li, "Application of a normalized difference impervious index (NDII) to extract urban impervious surface features based on Landsat TM images," *Int. J. Remote Sens.*, vol. 36, pp. 1055–1069, 2015.

[33] G. Sun *et al.*, "Combinational build-up index (CBI) for effective impervious surface mapping in urban areas," *IEEE J. Sel. Topics Appl. Earth Observ. Remote Sens.*, vol. 9, no. 5, pp. 2081–2092, May 2016.

[34] Z. Sun, C. Wang, H. Guo, and R. Shang, "A modified normalized difference impervious surface index (MNDISI) for automatic urban mapping from Landsat imagery," *Remote Sens.,* vol. 9, pp. 1–18, 2017.

[35] A. Garg, D. Pal, H. Singh, and D. C. Pandey, "A comparative study of NDBI, NDISI and NDII for extraction of urban impervious surface of Dehradun [Uttarakhand, India] using Landsat 8 imagery," in *Proc. IEEE Int. Conf. Emerg. Trends Commun. Technol.*, Dehradun, 2016, pp. 1–5, doi: 10.1109/ETCT.2016.7882963.

[36] A. Sekertekin, S. Abdikan, and A. M. Marangoz, "The acquisition of impervious surface area from LANDSAT 8 satellite sensor data using urban indices: A comparative analysis," *Environ. Monit. Assess.*, vol. 190, Jun. 2018, Art. no. 381.

[37] P. Tang *et al.*, "A novel sample selection method for impervious surface area mapping using JL1-3B nighttime light and Sentinel-2 imagery," *IEEE J. Sel. Topics Appl. Earth Observ. Remote Sens.*, vol. 13, pp. 3931–3941, Jun. 2020.

[38] J. Chen *et al.*, "A comparative study of impervious surface extraction using Sentinel-2 imagery," *Eur. J. Remote Sens.*, vol. 53, pp. 274–292, 2020.

[39] T. Jiang *et al.*, "Analysis of urban impervious surface in coastal cities: A case study in Lianyungang, China," in *Coastal Environment, Disaster, and Infrastructure - A Case Study of China's Coastline*. London, U.K.: IntechOpen, 2018, ch. 12, pp. 229–239.

[40] K. Rouibah and M. Belabbas, "Applying multi-index approach from Sentinel-2 imagery to extract urban areas in dry season (Semi-Arid land in north east Algeria)," *Revista De Teledeteccion*, vol. 56, pp. 89–101, 2020.

[41] A. Sekertekin, "Potential of global thresholding methods for the identification of surface water resources using Sentinel-2 satellite imagery and normalized difference water index," *J. Appl. Remote Sens.*, vol. 13, no. 1, 2019, Art. no. 044507.

[42] N. J. Valdiviezo, A. Tellez-Quinones, A. Salazar-Garibay, and A. A. Lopez-Caloca, "Built-up index methods and their applications for urban extraction from Sentinel 2A satellite data: Discussion," *J. Opt. Soc. Amer. A Opt. Image Sci. Vis.*, vol. 35, pp. 35–44, 2018.

[43] N. Otsu, "A threshold selection method from gray level histograms," *IEEE Trans. Syst., Man, Cybern*, vol. 9, no. 1, pp. 62–66, Jan. 1979.

[44] "National economic and social development statistics bulletin of Wuhan in 2019," *Wuhan Municipal Bur. Statist.*, 2019. [Online]. Available: http://tjj.wuhan.gov.cn/tjfw/tjgb/202004/t20200429_1191417.shtml. (accessed on 13 May 2020)

[45] M. Drusch *et al.*, "Sentinel-2: ESA's optical high-resolution mission for GMES operational services," *Remote Sens. Environ.*, vol. 120, pp. 25–36, 2012.

[46] Y. Xi, N. X. Thinh, and C. Li, "Preliminary comparative assessment of various spectral indices for built-up land derived from Landsat-8 OLI and Sentinel-2A MSI imageries," *Eur. J. Remote Sens.*, vol. 52, pp. 240–252, 2019.

[47] D. Frantz, E. Hass, A. Uhl, J. Stoffels, and J. Hill, "Improvement of the Fmask algorithm for Sentinel-2 images: Separating clouds from bright surfaces based on parallax effects," *Remote Sens. Environ.*, vol. 215, pp. 471–481, 2018.

[48] S. Qiu, Z. Zhu, and B. B. He, "Fmask 4.0: Improved cloud and cloud shadow detection in Landsats 4-8 and Sentinel-2 imagery," *Remote Sens. Environ.*, vol. 231, 2019, Art. no. 111205.

[49] L. Baetens, C. Desjardins, and O. Hagolle, "Validation of copernicus Sentinel-2 cloud masks obtained from MAJA, sen2cor, and FMask processors using reference cloud masks generated with a supervised active learning procedure," *Remote Sens.*, vol. 11, 2019, Art. no. 433.

[50] F. Ramoino, F. Tutunaru, F. Pera, and O. Arino, "Ten-meter Sentinel-2A cloud-free composite-southern Africa 2016," *Remote Sens,* vol. 9, 2017, Art. no. 652.

[51] R. Coluzzi, V. Imbrenda, M. Lanfredi, and T. Simoniello, "A first assessment of the Sentinel-2 level 1-C cloud mask product to support informed surface analyses," *Remote Sens. Environ.*, vol. 217, pp. 426–443, 2018.

[52] G. Wang, D. Garcia, Y. Liu, R. de Jeu, and A. Johannes Dolman, "A three-dimensional gap filling method for large geophysical datasets: Application to global satellite soil moisture observations," *Environ. Model. Softw.*, vol. 30, pp. 139–142, 2012.

[53] R. Nedkov, "Orthogonal transformation of segmented images from the satellite Sentinel-2," *Comptes Rendus De l'Acad. Bulgare Sci.*, vol. 70, no. 5, pp. 687–692, 2017.

[54] T. Shi and H. Xu, "Derivation of tasseled cap transformation coefficients for Sentinel-2 MSI at-sensor reflectance data," *IEEE J. Sel. Topics Appl. Earth Observ. Remote Sens.*, vol. 12, no. 10, pp. 4038–4048, Oct. 2019.

[55] B. Gao, "NDWI - A normalized difference water index for remote sensing of vegetation liquid water from space," *Remote Sens. Environ.*, vol. 58, pp. 257–266, 1996.

[56] A. R. Huete, "A soil adjusted vegetation index (SAVI)," *Remote Sens. Environ*, vol. 25, pp. 295–309, 1988.

[57] H. Xu, "Modification of normalised difference water index (NDWI) to enhance open water features in remotely sensed imagery," *Int. J. Remote Sens.*, vol. 27, pp. 3025–3033, 2006.

[58] A. Sekertekin, S. Y. Cicekli, and N. Arslan, "Index-based identification of surface water resources using Sentinel-2 satellite imagery," in *Proc. 2nd Int. Symp. Multidisciplinary Stud. Innov. Technol.*, Ankara, Turkey, 2018, pp. 1–5, doi: 10.1109/ISMSIT.2018.8567062.

[59] R. Bouhennache, T. Bouden, A. Taleb-Ahmed, and A. Cheddad, "A new spectral index for the extraction of built-up land features from Landsat 8 satellite imagery," *Geocarto Int,* vol. 34, no. 14, pp. 1531–1551, 2018.

[60] Y. Du *et al.*, "Water bodies' mapping from Sentinel-2 imagery with modified normalized difference water index at 10-m spatial resolution produced by sharpening the SWIR band," *Remote Sens,* vol. 8, 2016, Art. no. 354.

[61] G. Sun, H. Huang, Q. Weng, A. Zhang, X. Jia, J. Ren *et al.*, "Combinational shadow index for building shadow extraction in urban areas from Sentinel-2A MSI imagery," *Int. J. Appl. Earth Observ. Geoinf.*, vol. 78, pp. 53–65, 2019.

[62] Y. Zhou *et al.*, "Multiscale water body extraction in urban environments from satellite images," *IEEE J. Sel. Topics Appl. Earth Observ. Remote Sens.*, vol. 7, no. 10, pp. 4301–4312, Oct. 2014.

[63] J. Fan and B. Lei, "A modified valley-emphasis method for automatic thresholding," *Pattern Recognit. Lett.*, vol. 33, pp. 703–708, 2012.

[64] D. Sharma and J. Singhai, "An object-based shadow detection method for building delineation in high-resolution satellite images," *J. Photogramm. Remote Sens. Geoinf. Sci.*, vol. 87, pp. 103–118, 2019.

[65] M. I. Elbakary and K. M. Iftekharuddin, "Shadow detection of man-made buildings in high-resolution panchromatic satellite images," *IEEE Trans. Geosci. Remote Sens.*, vol. 52, no. 9, pp. 5374–5386, Sep. 2014.

[66] X. Huang and L. Zhang, "Morphological building/shadow index for building extraction from high-resolution imagery over urban areas," *IEEE J. Sel. Topics Appl. Earth Observ. Remote Sens.*, vol. 5, no. 1, pp. 161–172, Feb 2012.

Congmin Li is currently working toward the Ph.D. degree with the State Key Laboratory of Information Engineering in Surveying, Mapping and Remote Sensing, Wuhan University, Wuhan, China.

Her research interests include image processing and time-series image analysis.

Zhenfeng Shao received the Ph.D. degree in aerial photogrammetry from Wuhan University, Wuhan, China, in 2004.

He is currently a Professor with the State Key Laboratory of Information Engineering in Surveying, Mapping and Remote Sensing, Wuhan University. His research interests include remote sensing and environment monitoring.
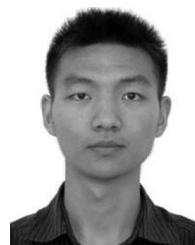

Lei Zhang received the Ph.D. degree in photogrammetry and remote sensing from Wuhan University, Wuhan, China, in 2017.

She is currently an Associate Research Fellow with the School of Remote Sensing and Information Engineering, Wuhan University, Wuhan, China. Her research interests include remote sensing image processing and time series analysis.

Xiao Huang received the Ph.D. degree in geography from the University of South Carolina, Columbia, SC, USA, in 2020.

He is an Assistant Professor with the Department of Geosciences, University of Arkansas. His research interests include GeoAI, big data, natural hazards, data science/visualization, and remote sensing.

Ming Zhang received the Ph.D. degree in earth system and geoinformation science from the Chinese University of Hong Kong, Hong Kong, in 2015.

His research interests include remote sensing of urban environments.